Supplementary Information

Revealing Hydrogen Spillover Pathways in Reducible Metal Oxides

Kazuki Shun,[a] Kohsuke Mori*[abc], Shinya Masuda,[a] Naoki Hashimoto,[a] Yoyo Hinuma,[d,] Hisayoshi Kobayashi,[e] and Hiromi Yamashita* [abc]

[a] Division of Materials and Manufacturing Science, Graduate School of Engineering, Osaka University, 2-1 Yamada-oka, Suita, Osaka 565-0871, Japan. Tel & FAX: +81-6-6879-7460, +81-6-6879-7457

E-mail: mori@mat.eng.osaka-u.ac.jp, yamashita@mat.eng.osaka-u.ac.jp

[b] Elements Strategy Initiative for Catalysts Batteries ESICB, Kyoto University, Katsura, Kyoto 615-8520, Japan.

[c] Innovative Catalysis Science Division, Institute for Open and Transdisciplinary Research Initiatives (ICS-OTRI), Osaka University, Suita, Osaka 565-0871, Japan.

[d] Department of Energy and Environment, National Institute of Advanced Industrial Science and Technology (AIST), Ikeda, Osaka 563-8577, Japan

[e] Kyoto Institute of Technology, Matsugasaki, Sakyo-ku, Kyoto 606-8585, Japan.

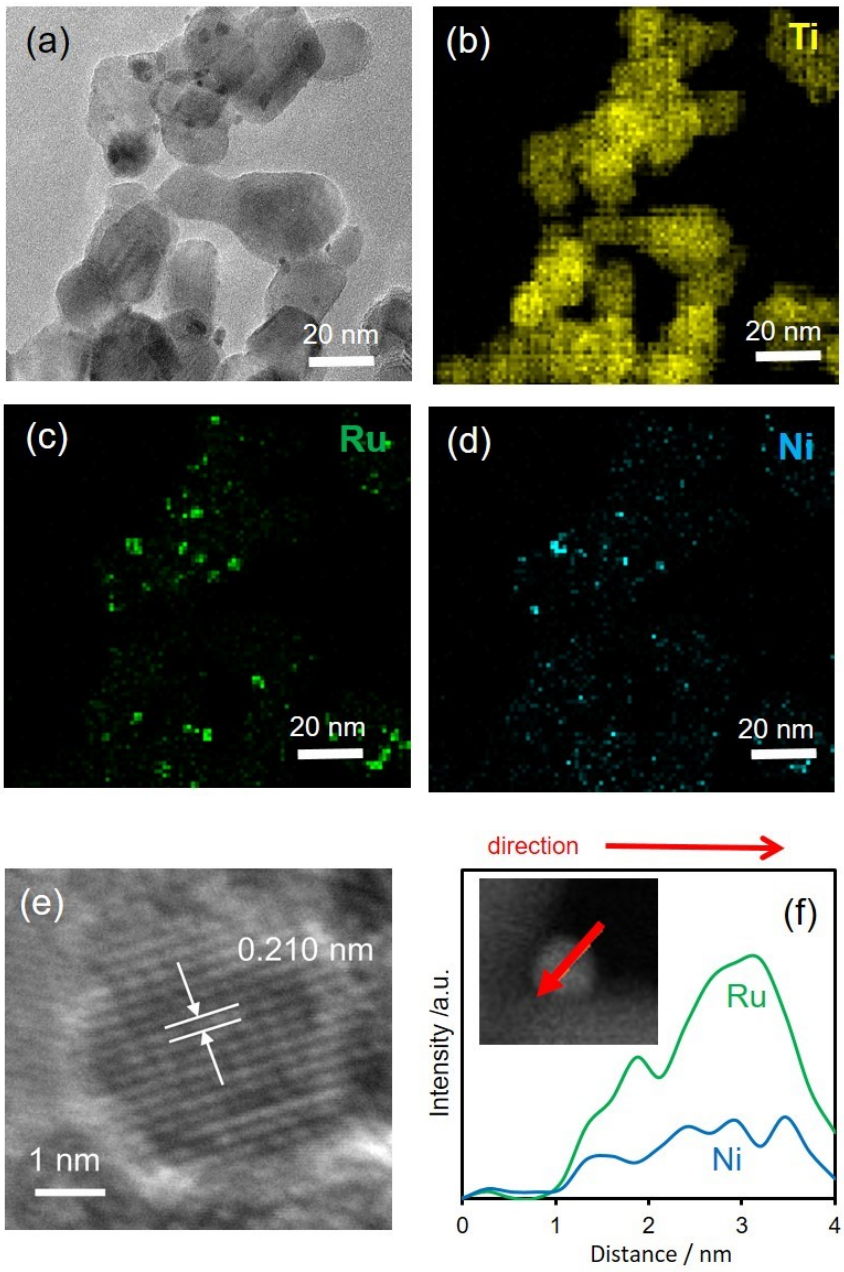

Fig. S1. (a) TEM image of RuNi/TiO_2, EDX mapping of (b) Ti, (c) Ru, (d) Ni in the region indicated in (a), (e) lattice fringe of RuNi NP observed in the HR-TEM image, and (f) EDX line analysis of single nanoparticle.

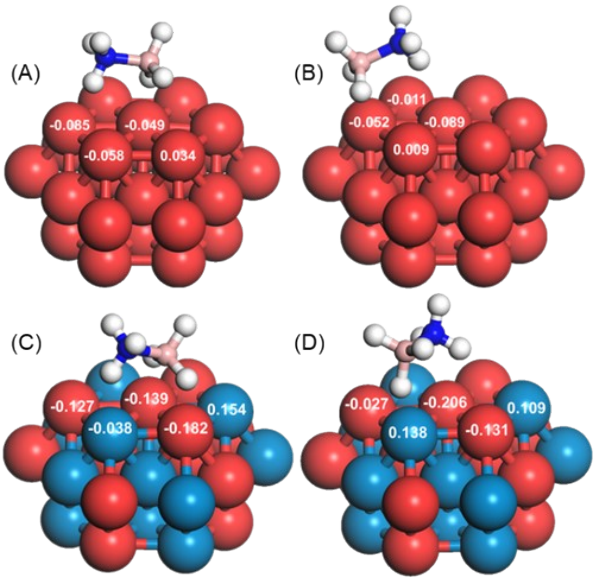

Sample		Adsorption Energy of AB [kcal·mol]	HOMO level [eV]
Ru_{26} Cluster		-	−3.72
$Ru_{13}Ni_{13}$ Cluster		-	−3.60
Ru_{26}	(A) Ru_C−B	7.5	−3.52
	(B) Ru_C−N	19.3	−3.51
$Ru_{13}Ni_{13}$	(C) Ru_C−B	27.7	−3.37
	(D) Ru_C−N	31.7	−3.46

Fig. S2. Geometrically optimized adsorption energies of AB molecule on the Ru_{26} or $Ru_{13}Ni_{13}$ alloy cluster and HOMO level of each condition estimated from DFT calculations. Ru_{26} cluster is used as the model in the case of (A), (B), and $Ru_{13}Ni_{13}$ alloy cluster is used in the case of (C), (D).

DFT calculations, employing a Ru_{26} and $Ru_{13}Ni_{13}$ clusters as models of monometallic and alloy NPs, revealed that Ru atoms in the $Ru_{13}Ni_{13}$ clusters are indeed negatively charged in comparison with Ru_{26} cluster, while the Ni atoms have positive charges due to the electronic charge transfer from Ni to Ru. Additionally, the highest occupied molecular orbital (HOMO) state of the $Ru_{13}Ni_{13}$ cluster is higher than that of monometallic Ru_{26} cluster, which is calculated to be − 3.60 eV and − 3.71 eV, respectively. The change of electronic property by alloying also influences on the adsorption energy (E_{ad}) of AB molecules. In the lowest-energy adsorption structure for Ru_{26} cluster, AB interacts with surface Ru atoms through the boron atom and the centered Ru atom (Ru_c), in which E_{ad} was estimated to be 7.5 kcal/mol (Fig. S2A). The opposite configuration is more stable and the E_{ad} was estimated to be 19.3 kcal/mol (Fig. S2B). As expected, the E_{ad} of both configurations for the $Ru_{13}Ni_{13}$ cluster were estimated to be 27.7 and 31.7 kcal/mol, respectively (Fig. 2C and D), which are substantially larger than those on the Ru_{26} cluster. Thus we can conclude that the neighboring Ru−Ni paired site with unique electronic property has a positive effect as an anchor on interaction with AB molecules, which ultimately enhances the catalytic activity.

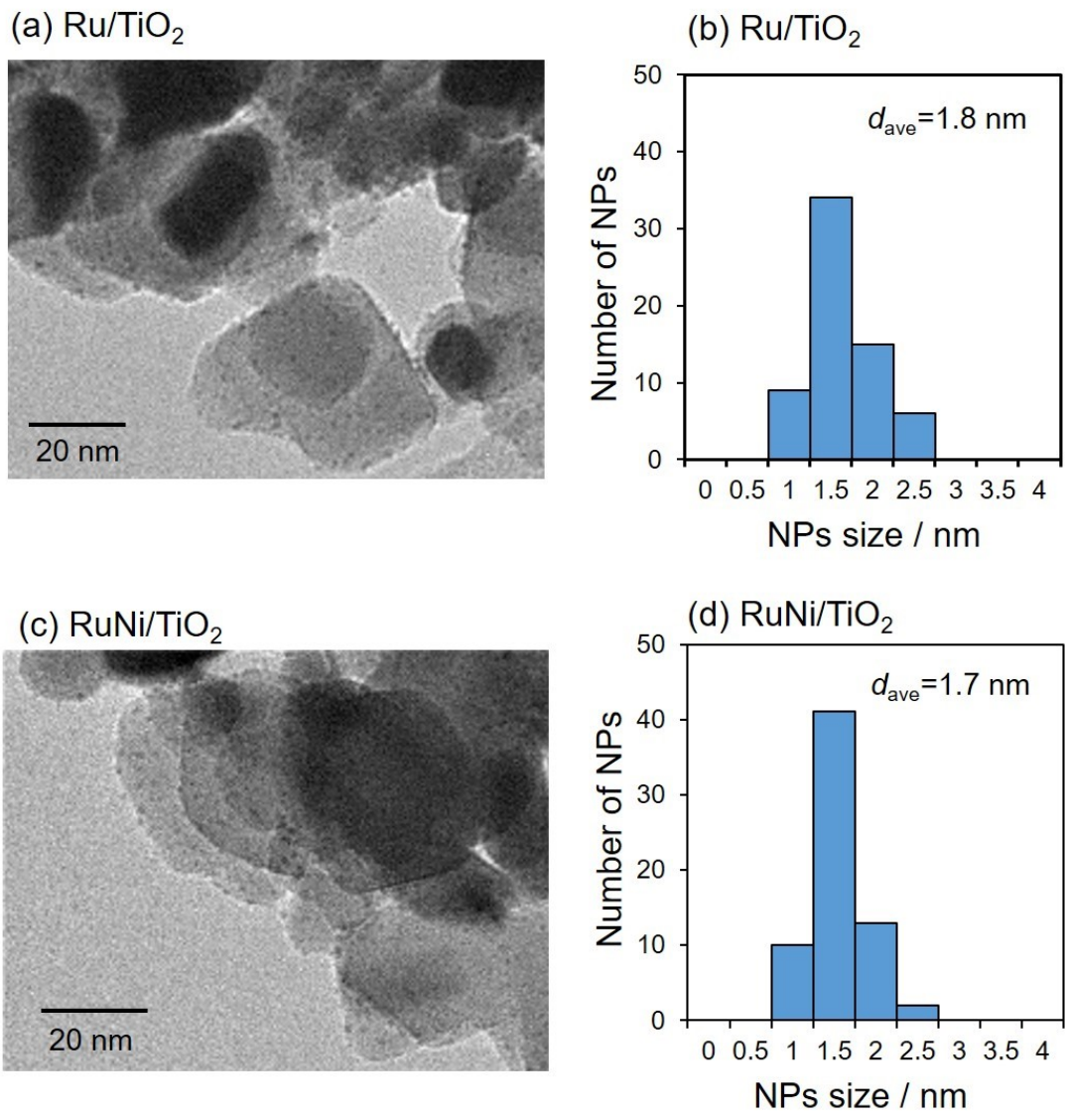

Fig. S3. TEM images and size distributions of metal NPs supported on TiO_2.

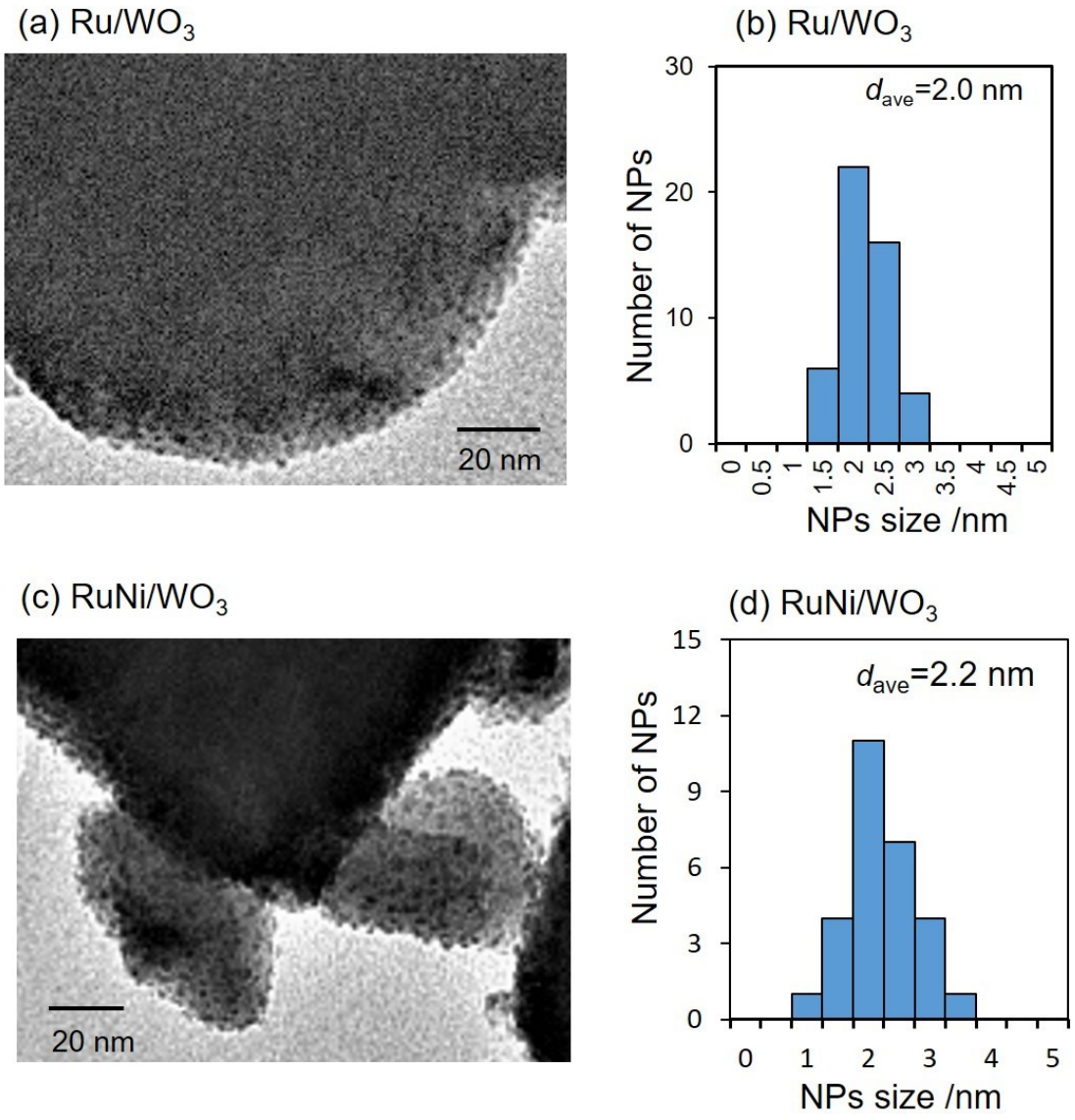

Fig. S4. TEM images and size distributions of metal NPs supported on WO_3.

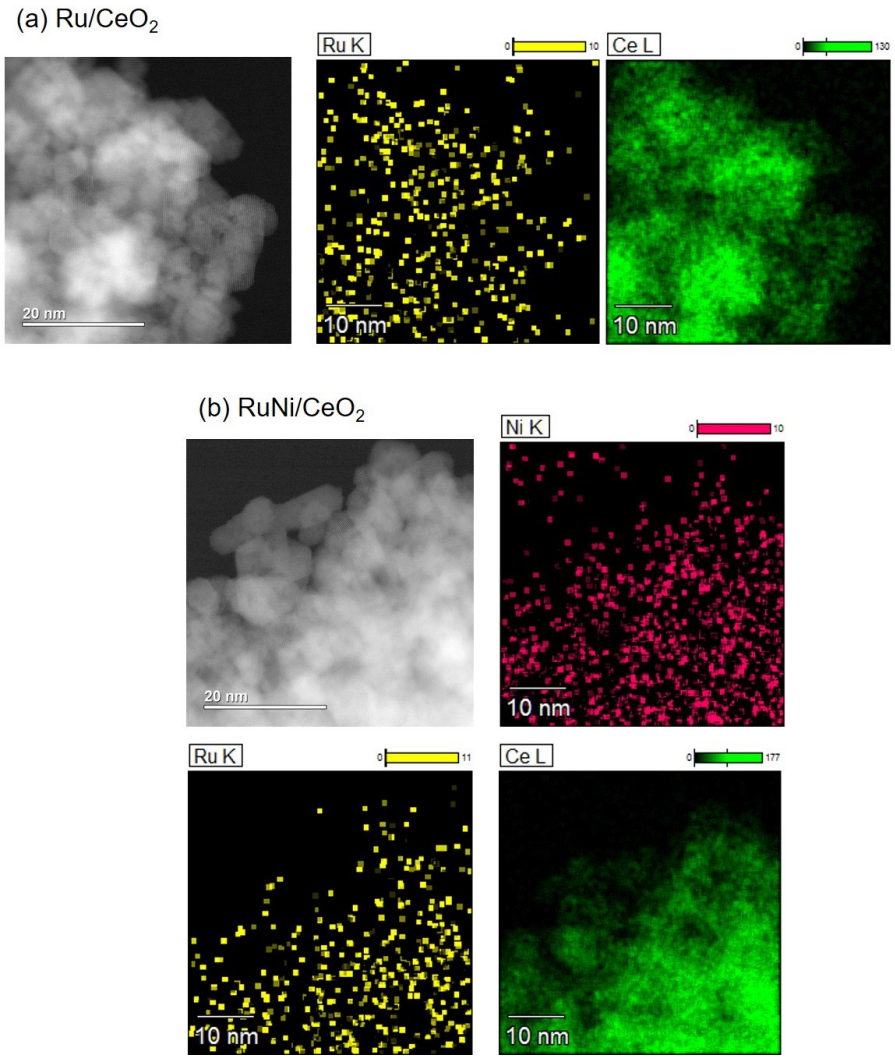

Fig. S5. HAADF-STEM images and elemental mapping of (a) Ru/CeO_2 and (b) $RuNi/CeO_2$.

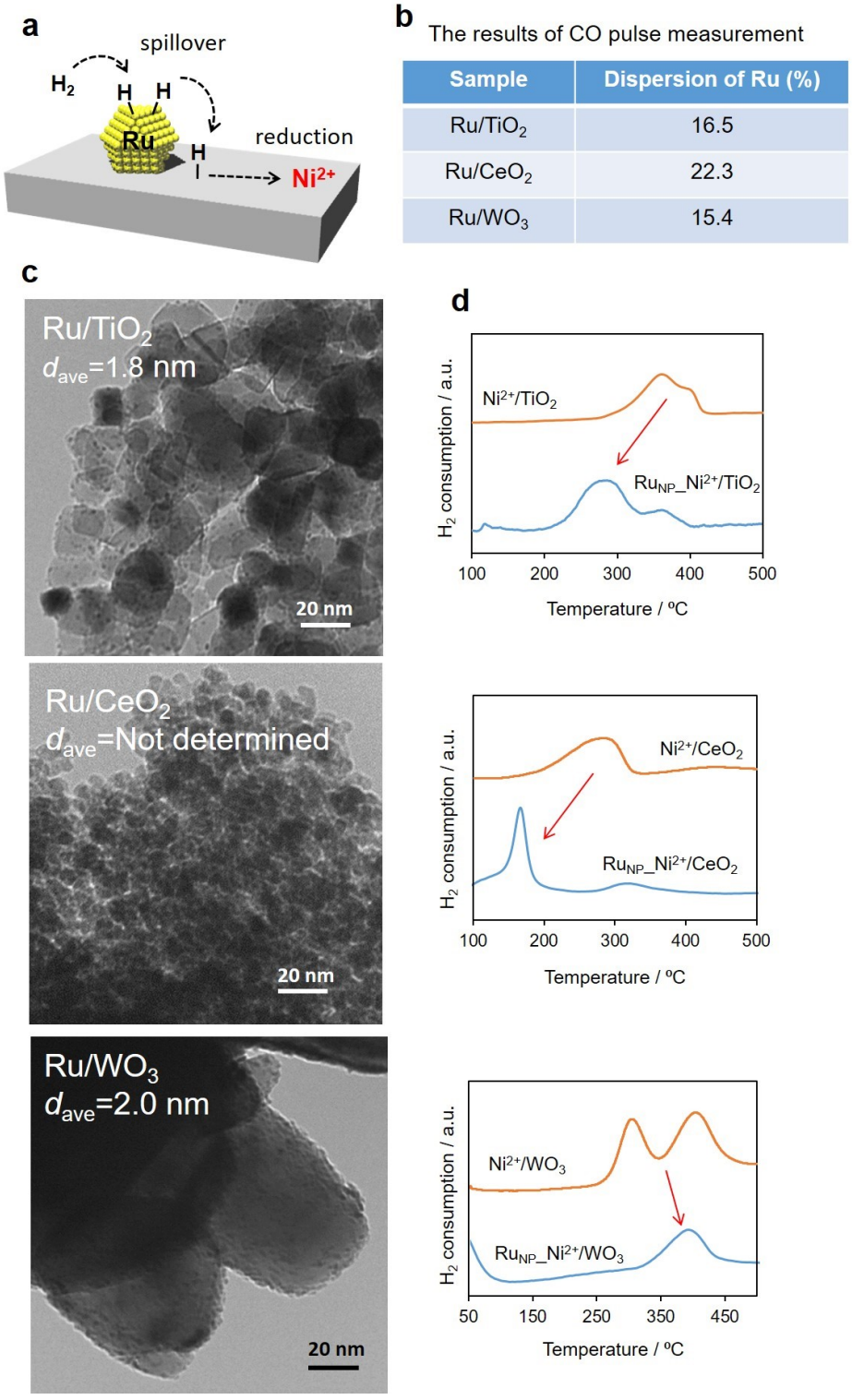

Fig. S6. (**a**) Schematic image of the experiment for the reduction of deposited Ni^{2+} ions by the spilled H atoms from pre-reduced Ru NPs, (**b**) the dispersion of Ru determined by CO pulse measurement, (**c**) TEM images of pre-reduced Ru/TiO_2, Ru/CeO_2, and Ru/WO_3, and (**d**) comparison of H_2-TPR results for Ni^{2+}-deposited samples and pre-reduced Ru NPs and Ni^{2+}-deposited samples.

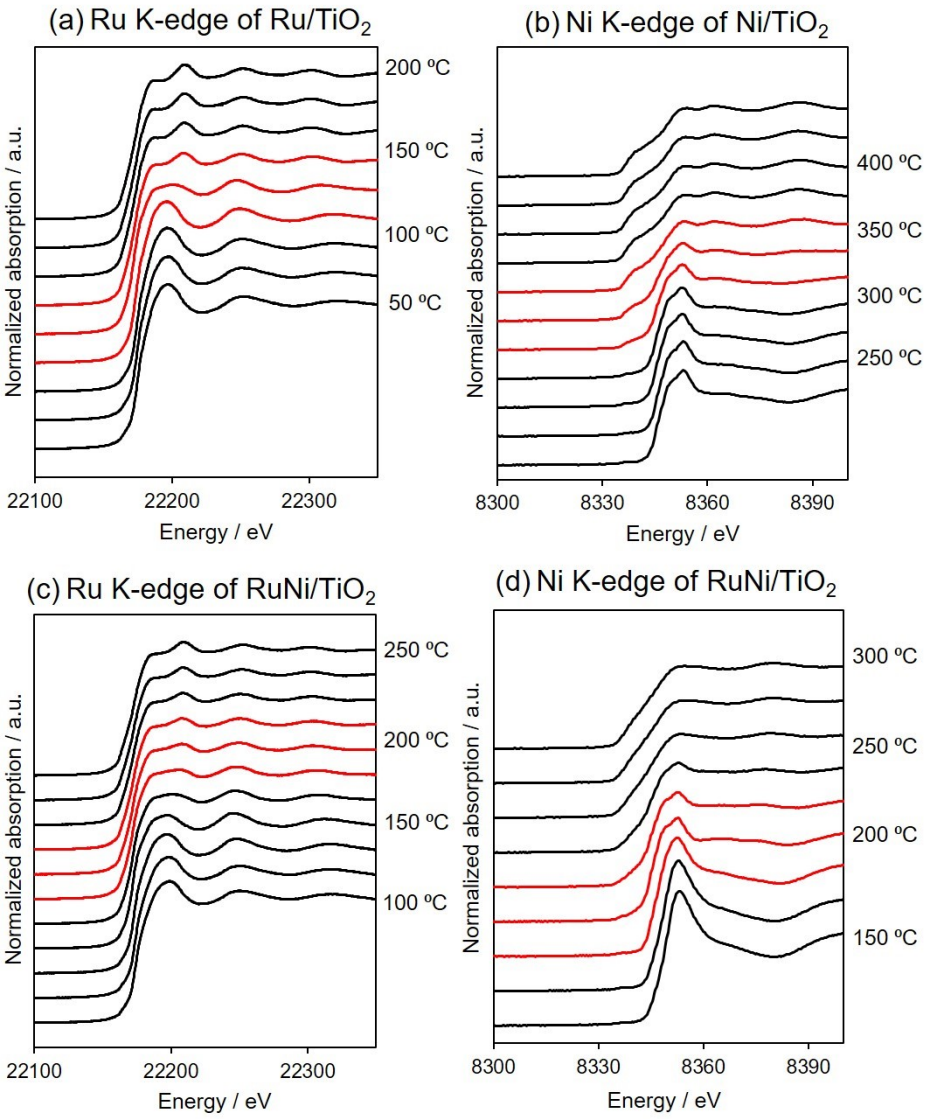

Fig. S7. Ru K-edge XANES spectra of (a) Ru/TiO_2 and (c) $RuNi/TiO_2$ and Ni K-edge XANES spectra of (b) Ni/TiO_2 and (d) $RuNi/TiO_2$.

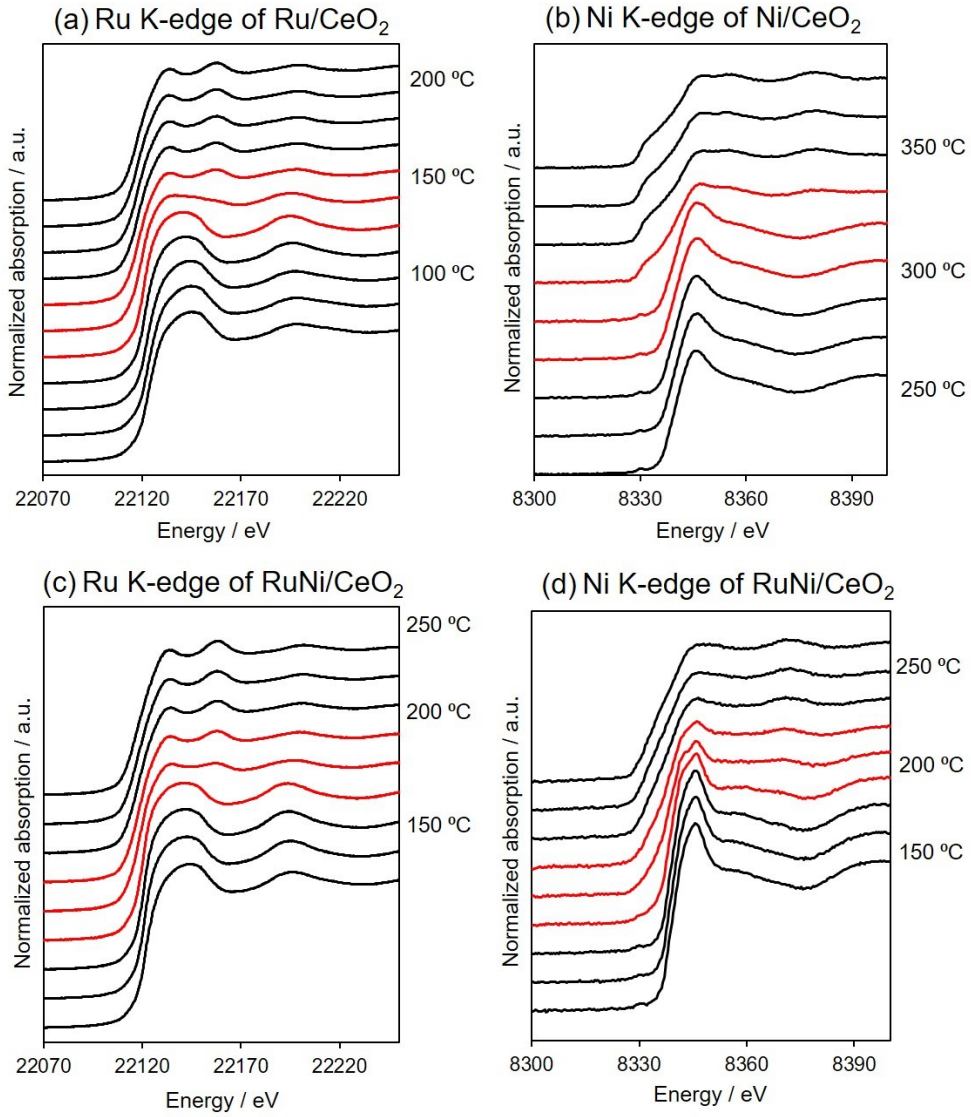

Fig. S8 Ru K-edge XANES spectra of (a) Ru/CeO_2 and (c) $RuNi/CeO_2$ and Ni K-edge XANES spectra of (b) Ni/CeO_2 and (d) $RuNi/CeO_2$.

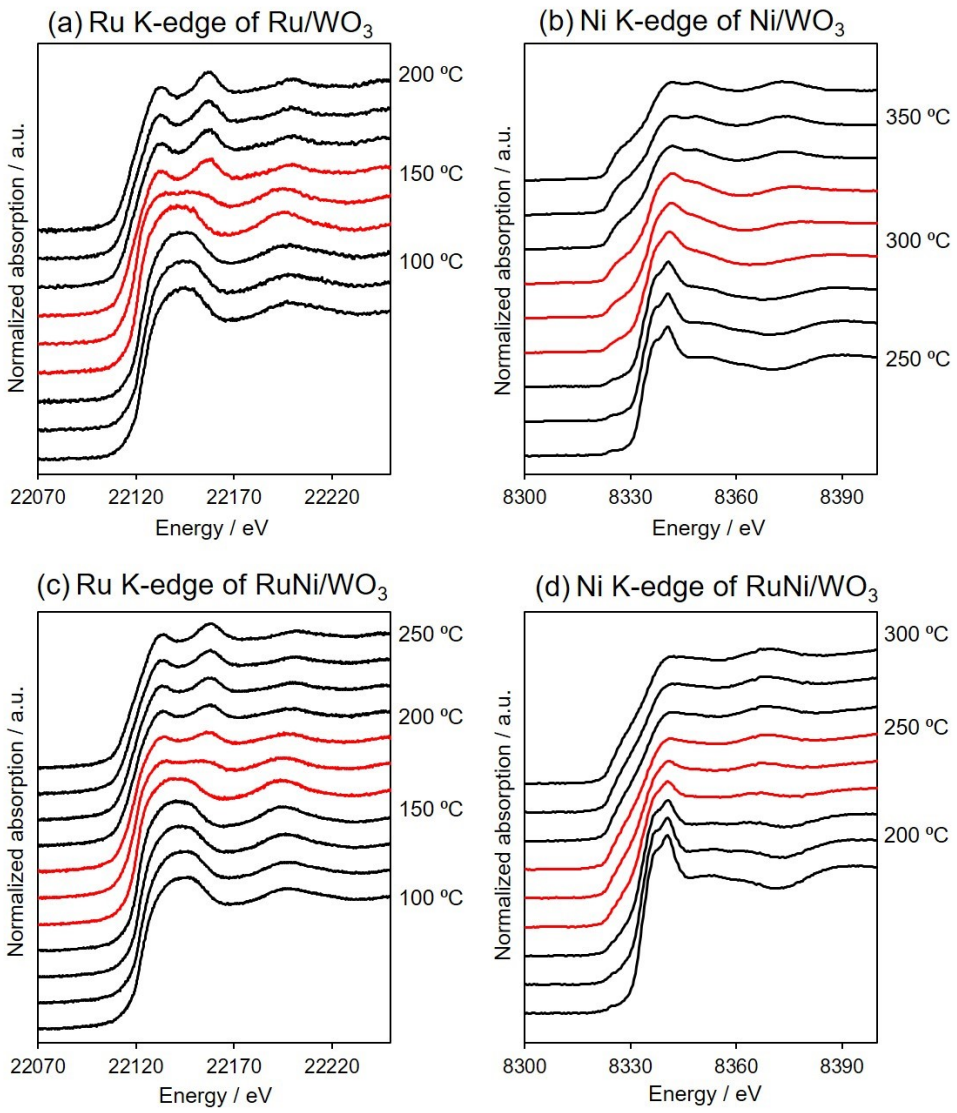

Fig. S9 Ru K-edge XANES spectra of (a) Ru/WO_3, (c) $RuNi/WO_3$, and Ni K-edge XANES spectra of (b) Ni/WO_3 and (d) $RuNi/WO_3$.

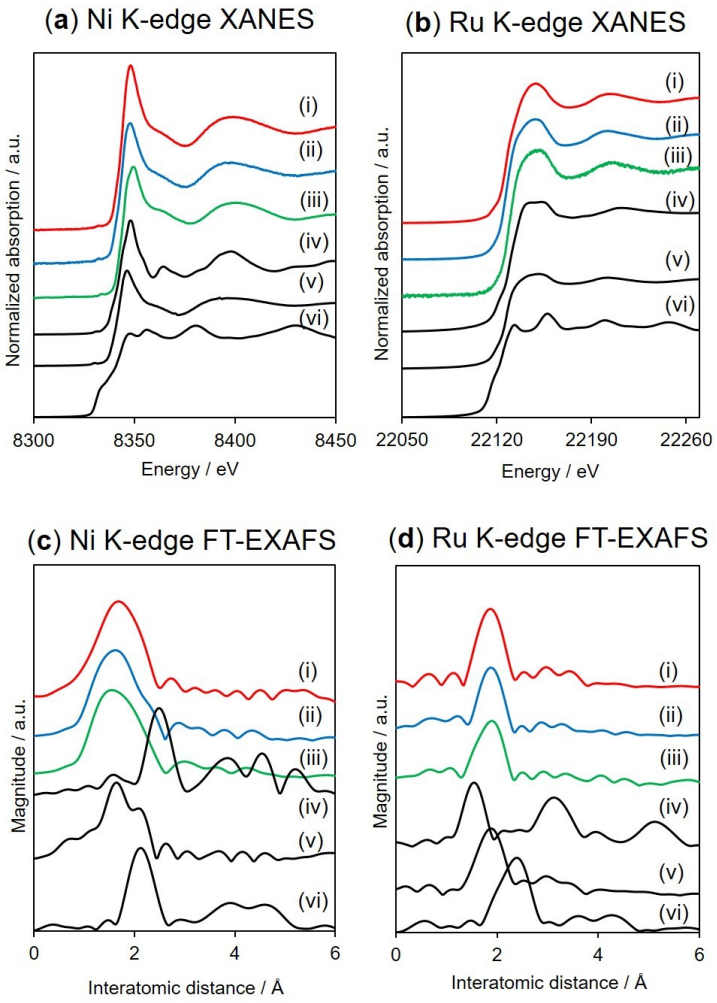

Fig. S10 Ni K-edge (a) XANES and (c) FT-EXAFS spectra of as deposited (i) RuNi/TiO_2, (ii) RuNi/CeO_2, (iii) RuNi/WO_3, and reference samples (iv) NiO, (v) $NiCl_2$, and (vi) Ni foil. Ru K-edge (b) XANES and (d) FT-EXAFS spectra of as deposited (i) RuNi/TiO_2, (ii) RuNi/CeO_2, (iii) RuNi/WO_3, and reference samples (iv) RuO_2, (v) $RuCl_3$, and (vi) Ru foil.

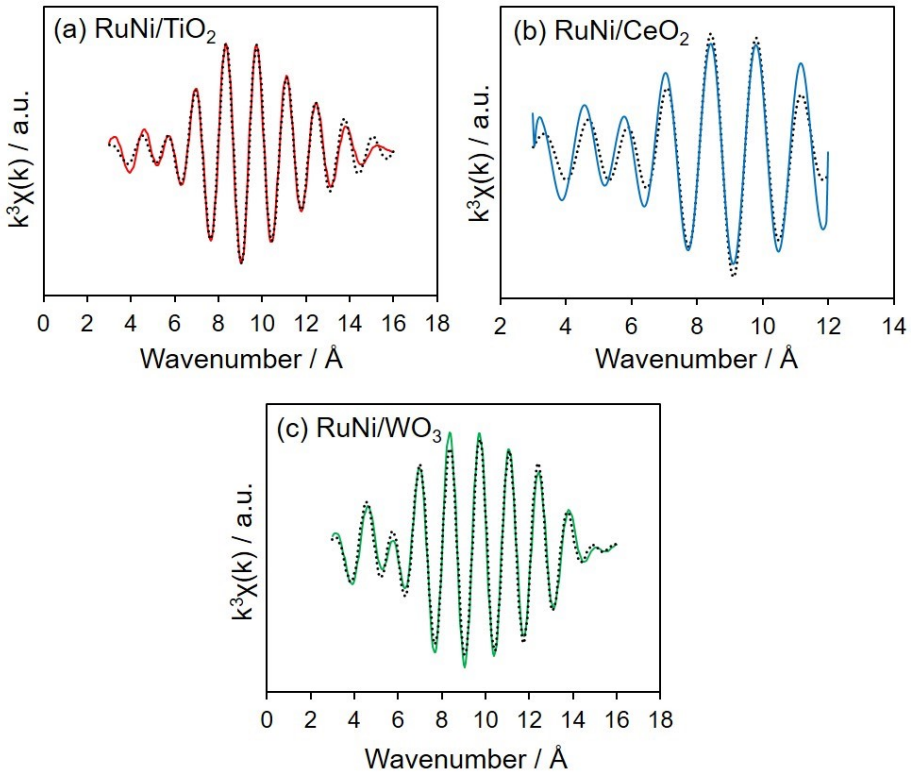

Fig. S11 Inverse-FT of Ru K-edge k^3-weighted EXAFS (black dot) and Curve-fitting result for (a) RuNi/TiO_2, (b) RuNi/CeO_2, and (c) RuNi/WO_3.

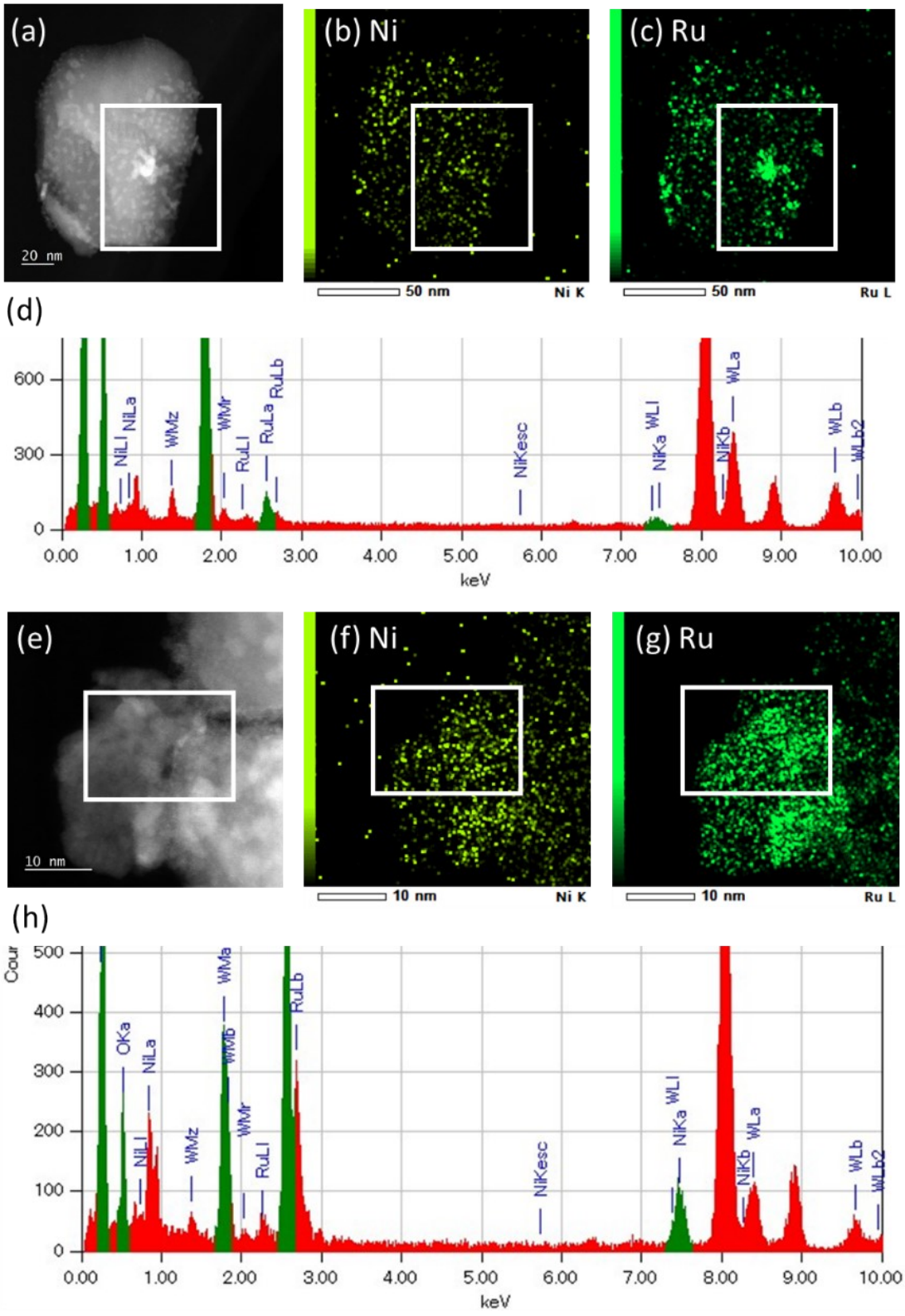

Fig. S12. HAADF-STEM images (a and e) and elemental mapping of RuNi/WO_3 of Ru (b and f), Ni (c and g), and EDX analysis (d and h) in the indicated region.

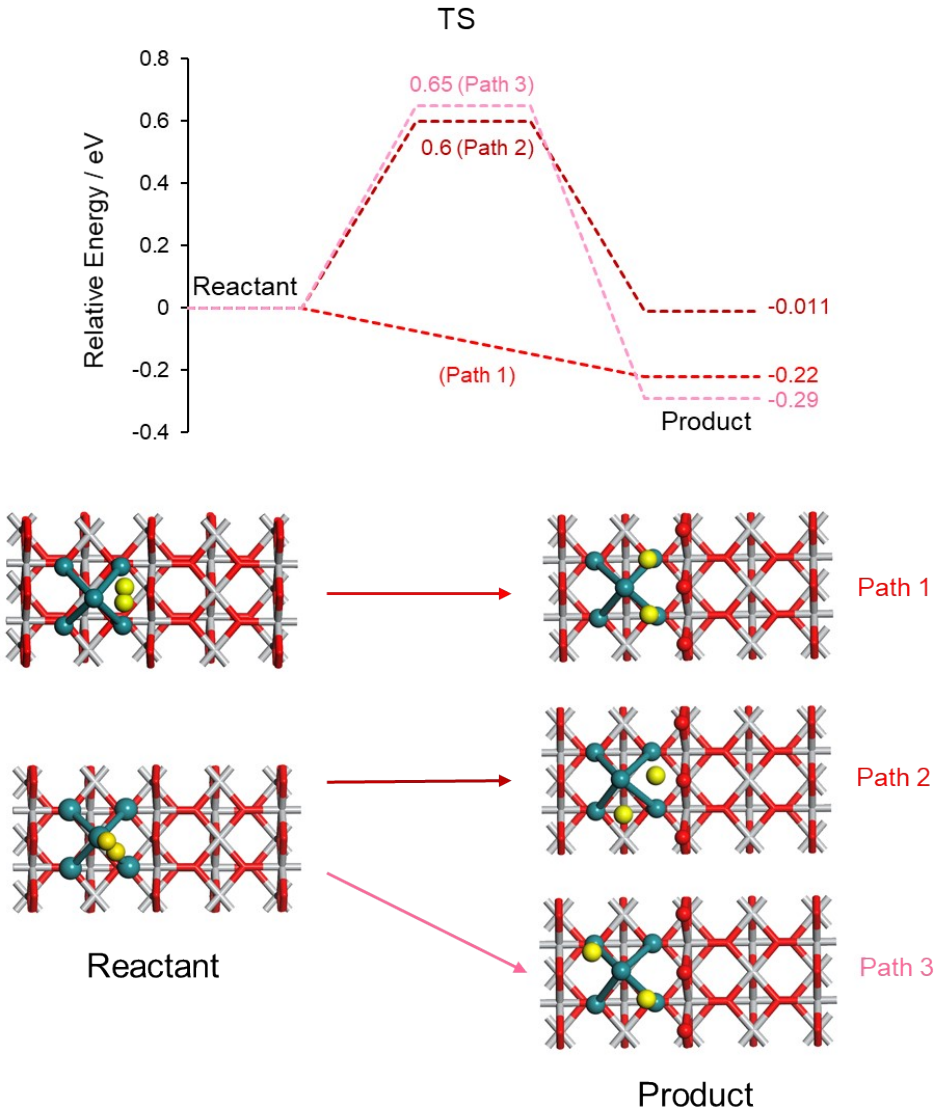

Fig. S13. Energy profiles and calculated model for H_2 cleavage on Ru5(homolytic) (Step 1) on TiO_2(110). Green ball (Ru), yellow ball (H), red stick (O), and gray stick (Ti).

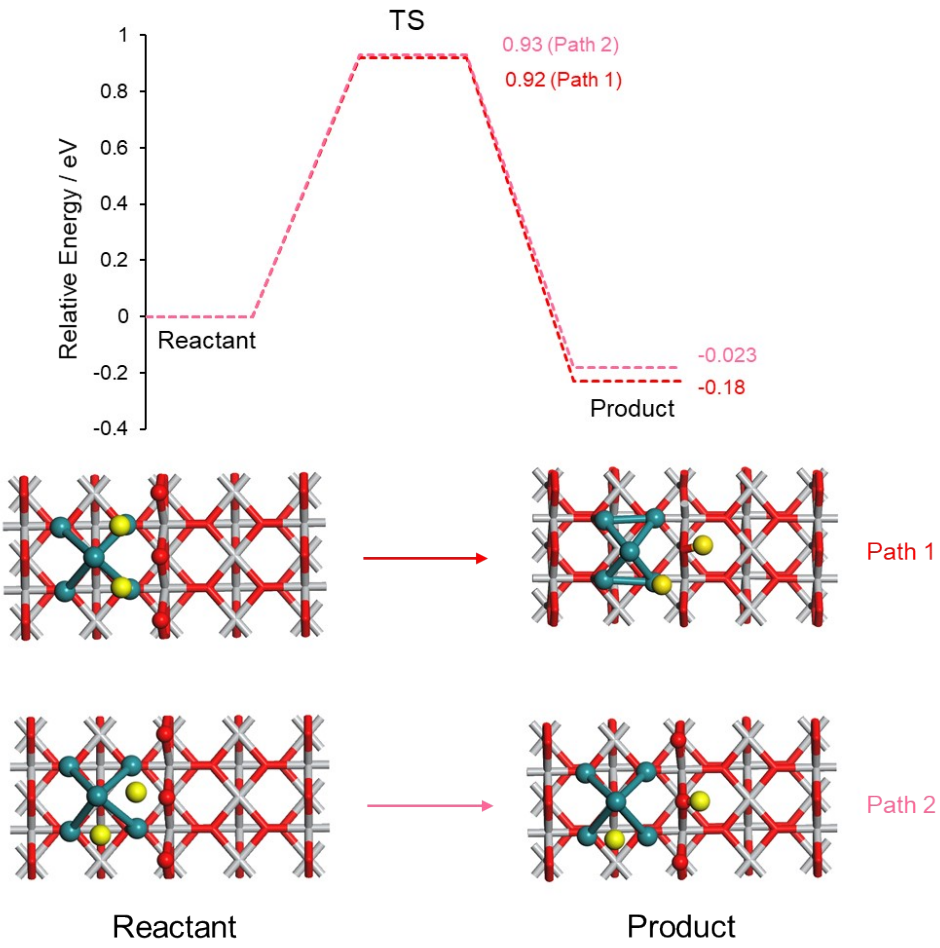

Fig. S14. Energy profiles and calculated model for H atom transfer from Ru_5 to oxide (Step 2) on TiO_2(110). Green ball (Ru), yellow ball (H), red stick (O), and gray stick (Ti).

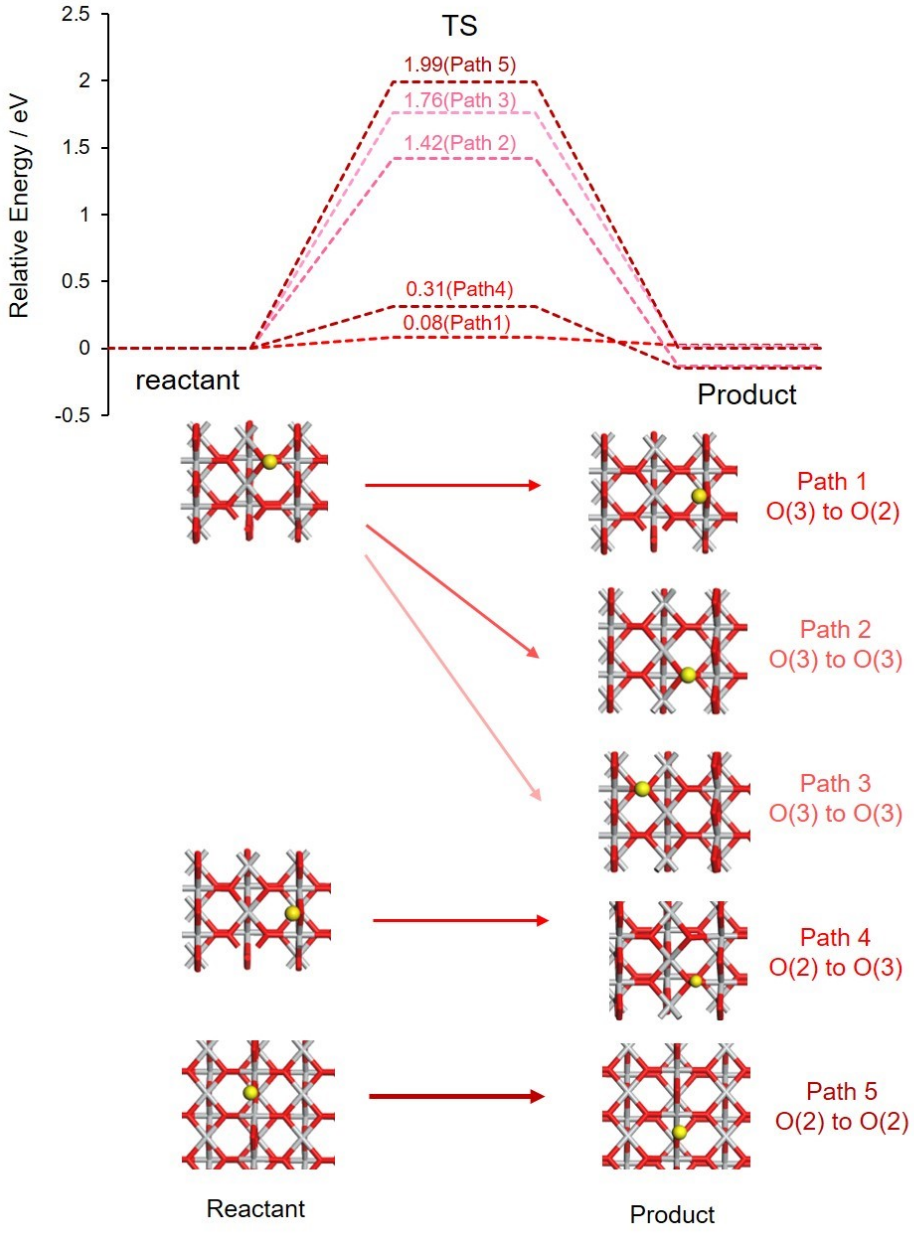

Fig. S15. Energy profiles and calculated models for H atom migration (Step 3) on TiO_2(110). Yellow ball (H), red stick (O), and gray stick (Ti).

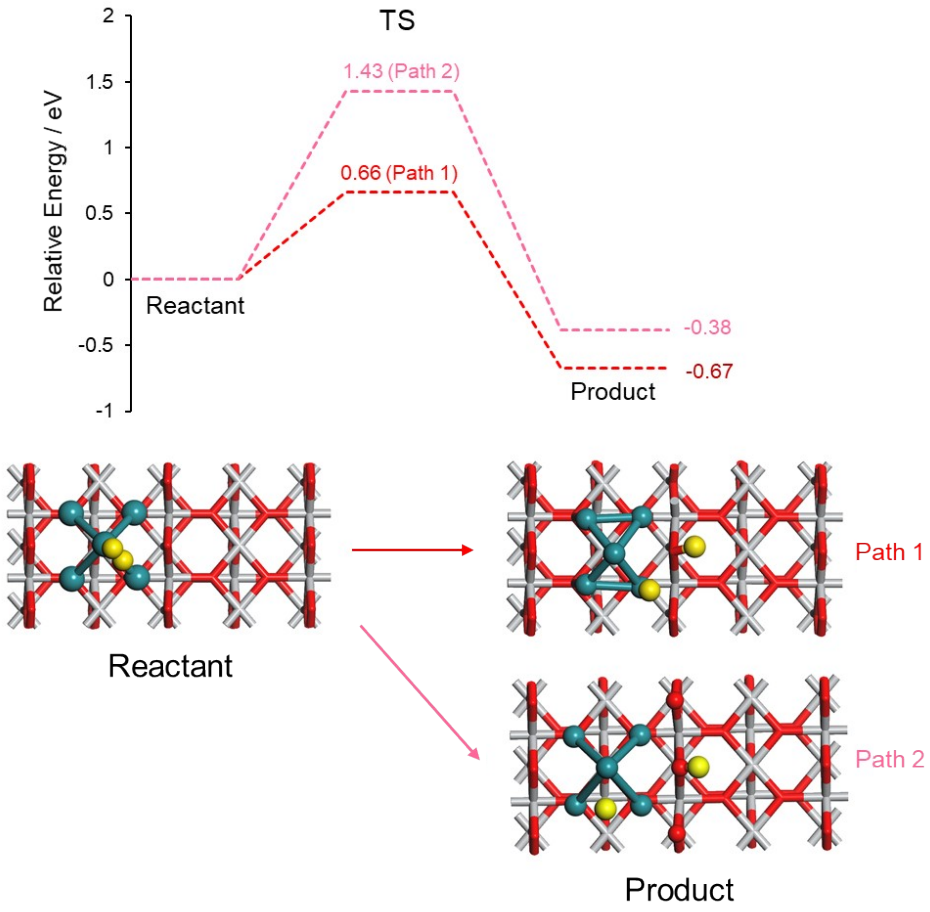

Fig. S16. Energy profiles and calculated model for H_2 cleavage on Ru_5 and oxide (heterolytic) (Step 1') on TiO_2(110). Green ball (Ru), yellow ball (H), red stick (O), and gray stick (Ti).

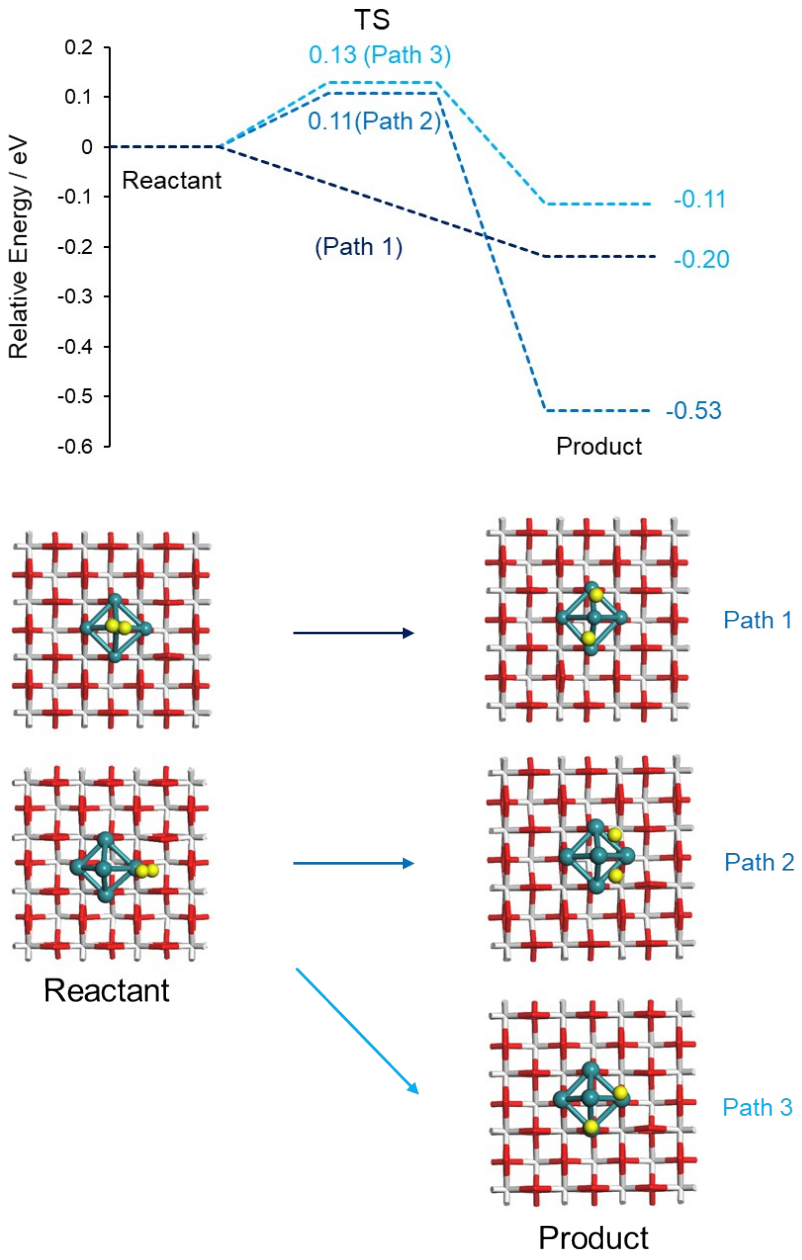

Fig. S17. Energy profiles and calculated model the H_2 cleavage on Ru5(homolytic) (Step 1) on CeO_2(100). Green ball (Ru), yellow ball (H), red stick (O), and white stick (Ce)

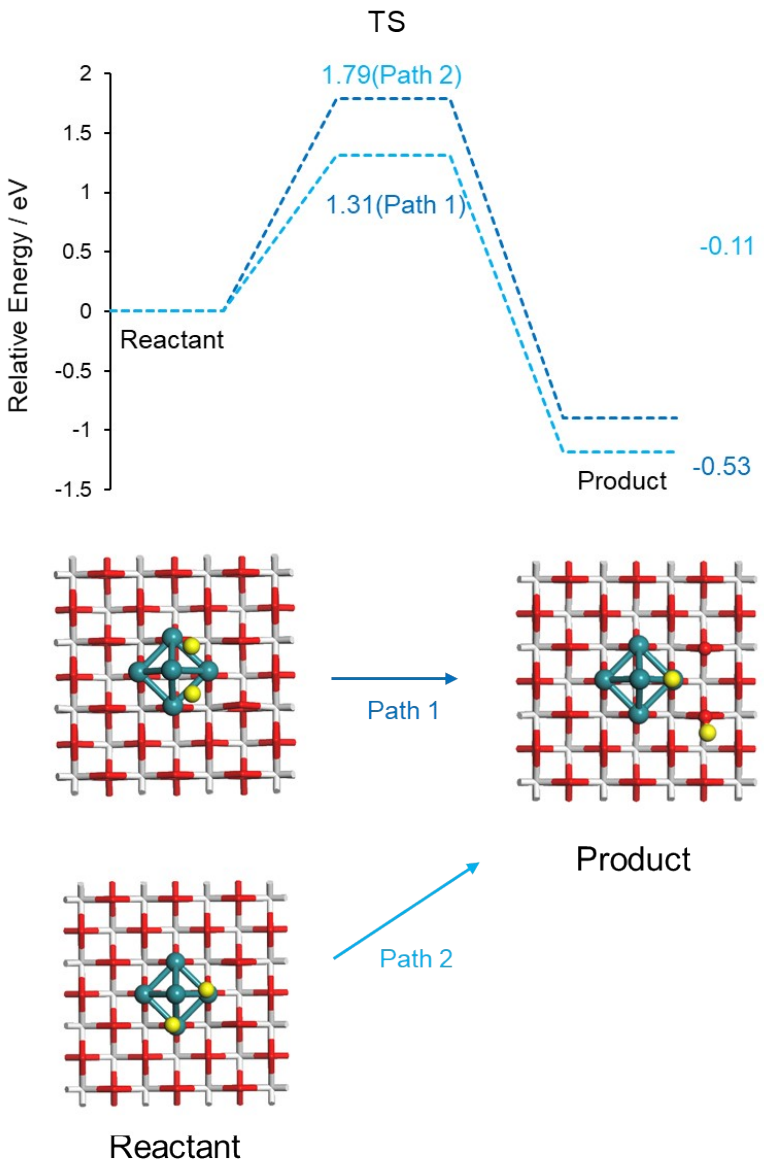

Fig. S18. Energy profiles and calculated model for H atom transfer from Ru_5 to oxide (Step 2) on CeO_2(100). Green ball (Ru), yellow ball (H), red stick (O), and white stick (Ce)

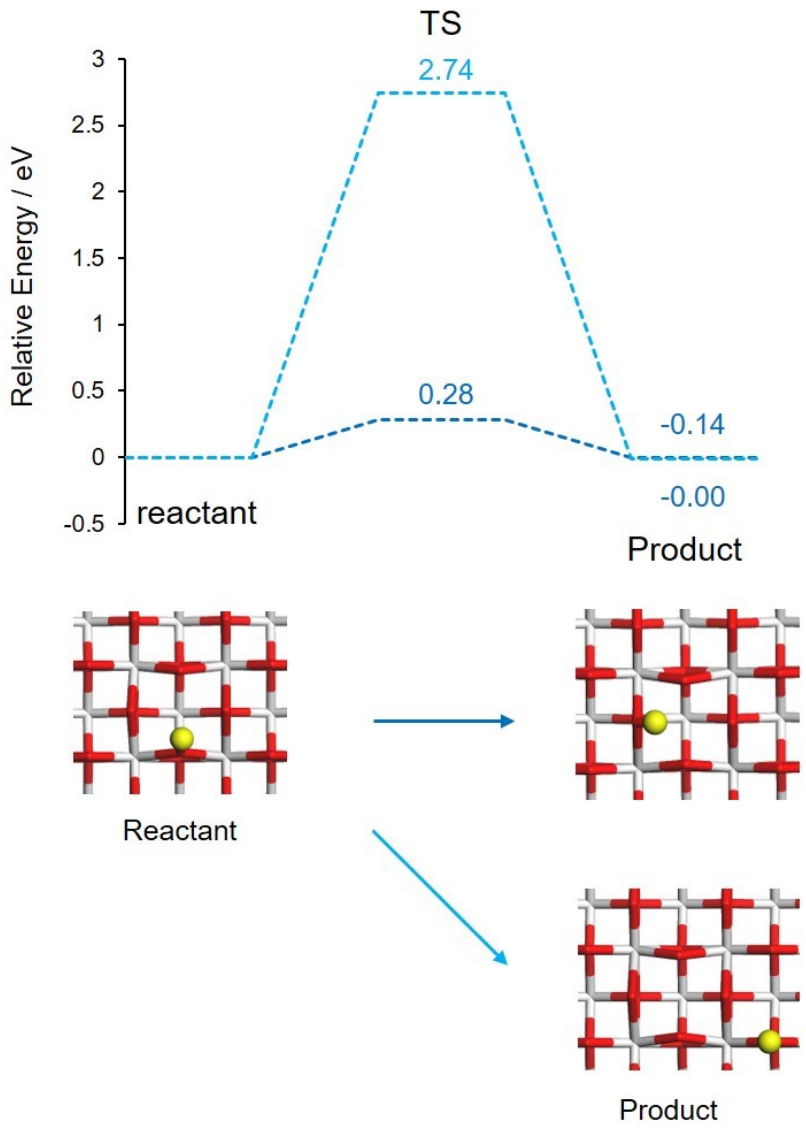

Fig. S19. Energy profiles and calculated models for e H atom migration (Step 3) on CeO_2(001). Yellow ball (H), red stick (O), and white stick (Ce).

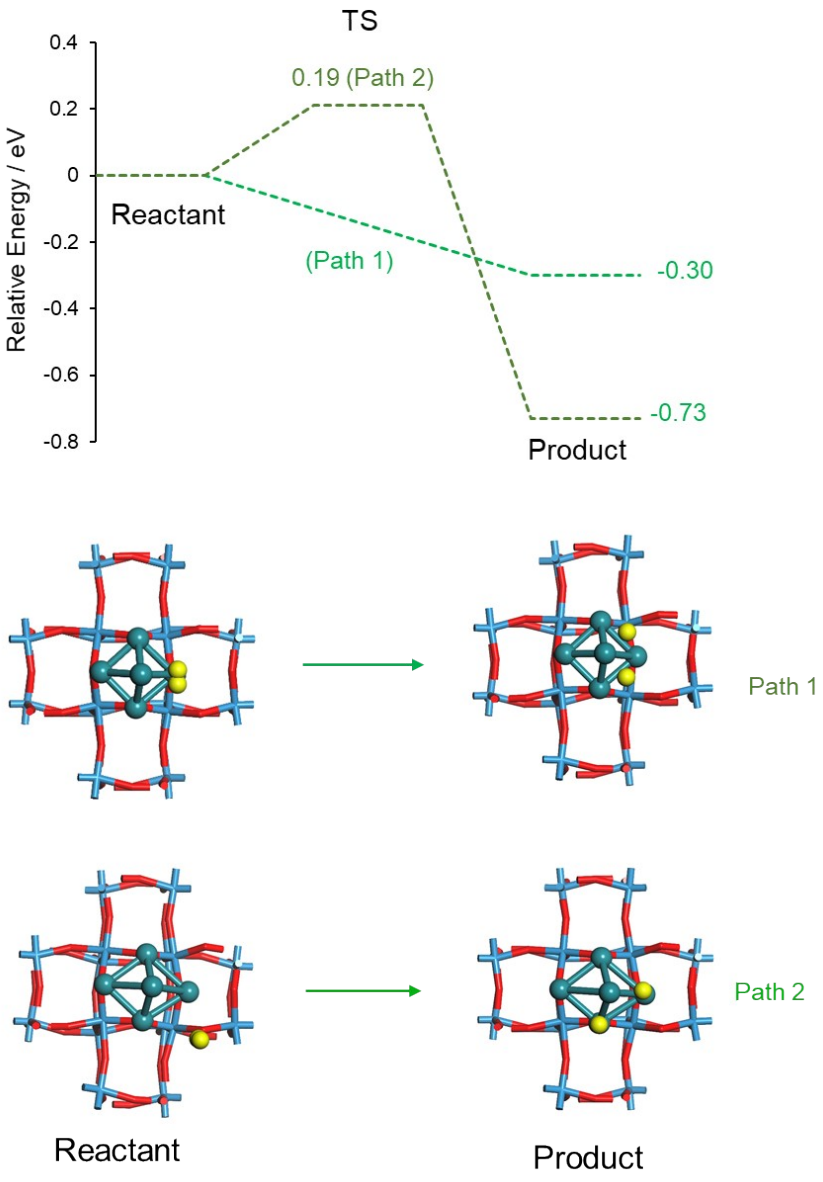

Fig. S20. Energy profiles and calculated model for H_2 cleavage on Ru5(homolytic) (Step 1) on WO_3 (001). Green ball (Ru), yellow ball (H), red stick (O), and blue stick (W).

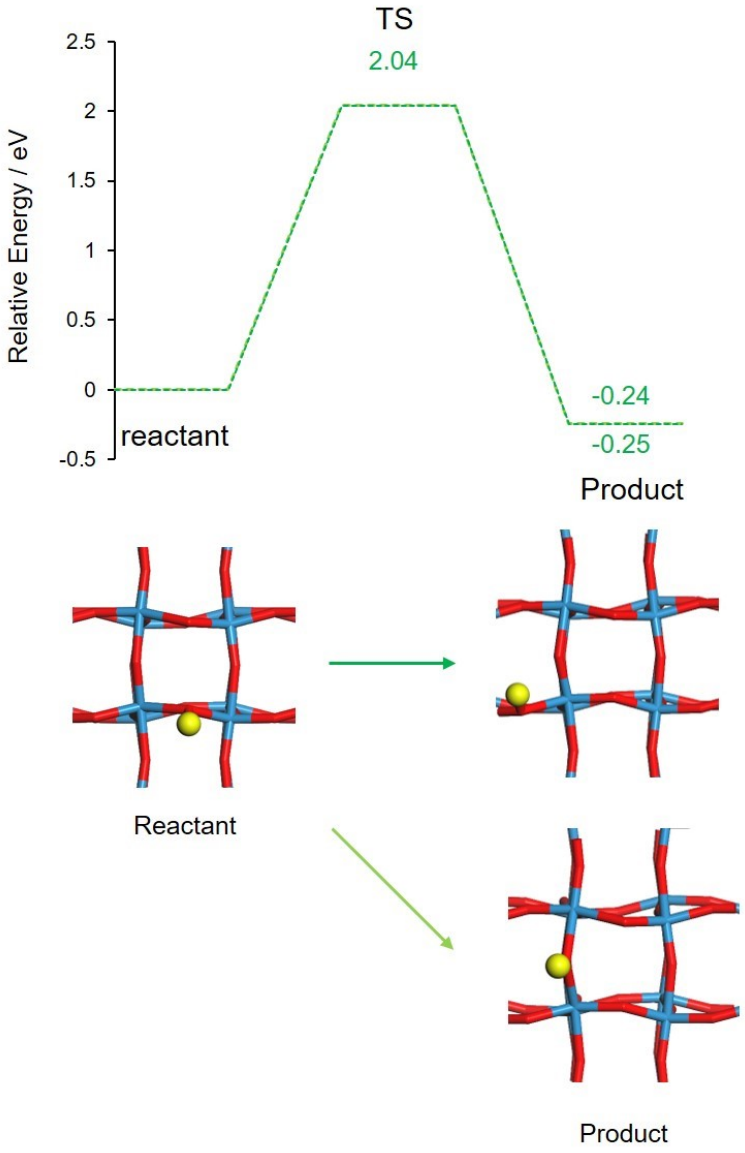

Fig. S21. Energy profiles and calculated models for H atom migration (Step 3) on WO_3(001). Yellow ball (H), red stick (O), and blue stick (W).

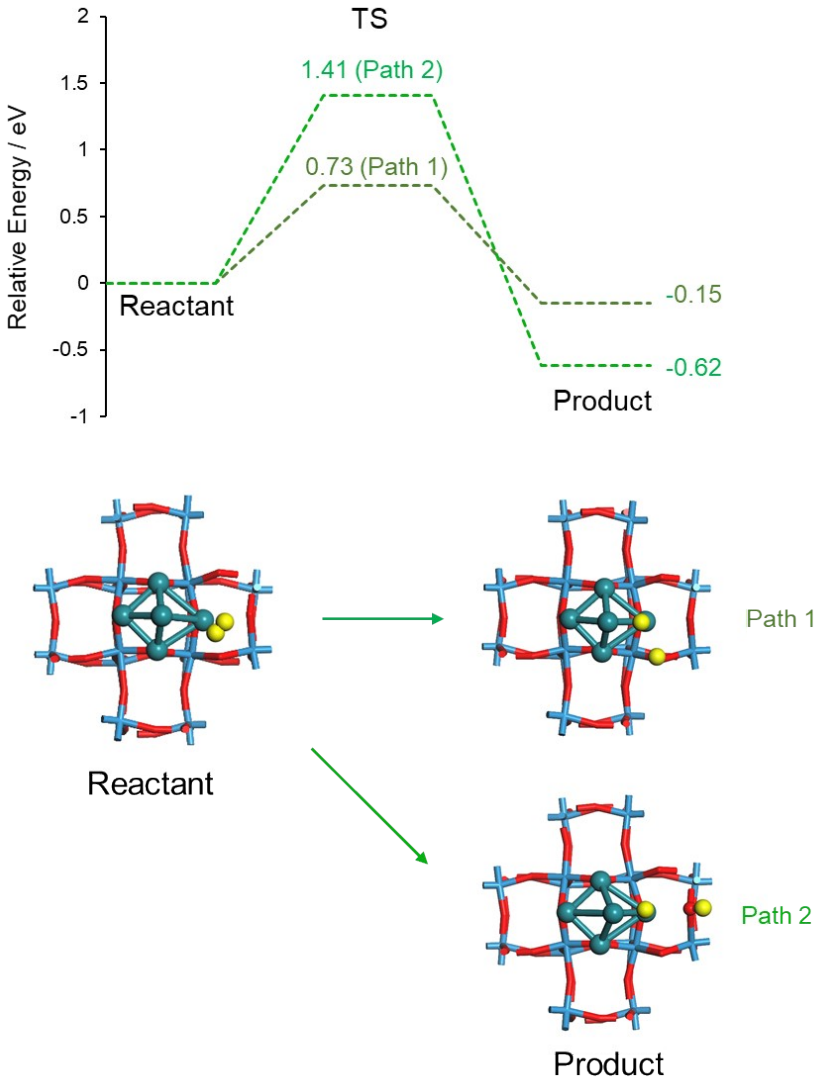

Fig. S22. Energy profiles and calculated model for H_2 cleavage on Ru_5 and oxide (heterolytic) (Step 1') on WO_3(001). Green ball (Ru), yellow ball (H), red stick (O), and blue stick (W).

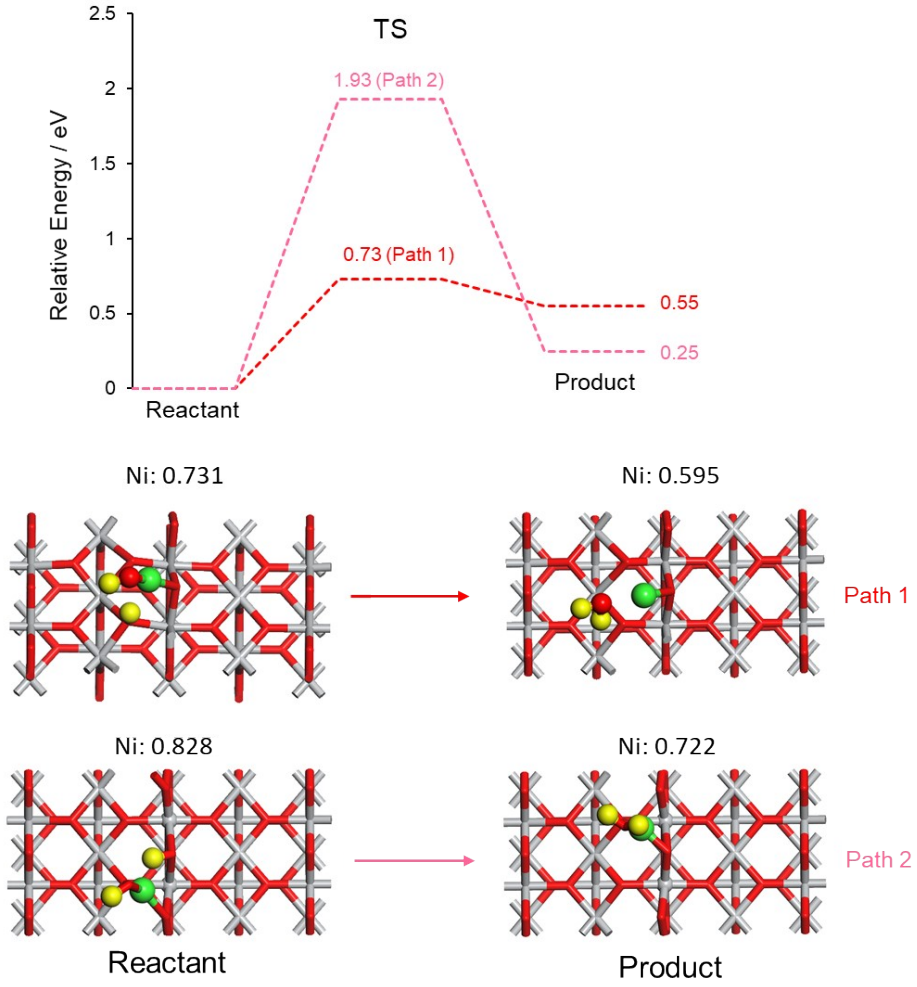

Fig. S23. Energy profiles and calculated model for reduction of Ni^{n+} by spilled H (Langmuir–Hinshelwood mechanism) (Step 4) on TiO_2(110). The values in the models are Mulliken atomic charges of Ni atom as determined by DFT calculations. Pale green ball (Ni), yellow ball (H), red stick (O), and gray stick (Ti)

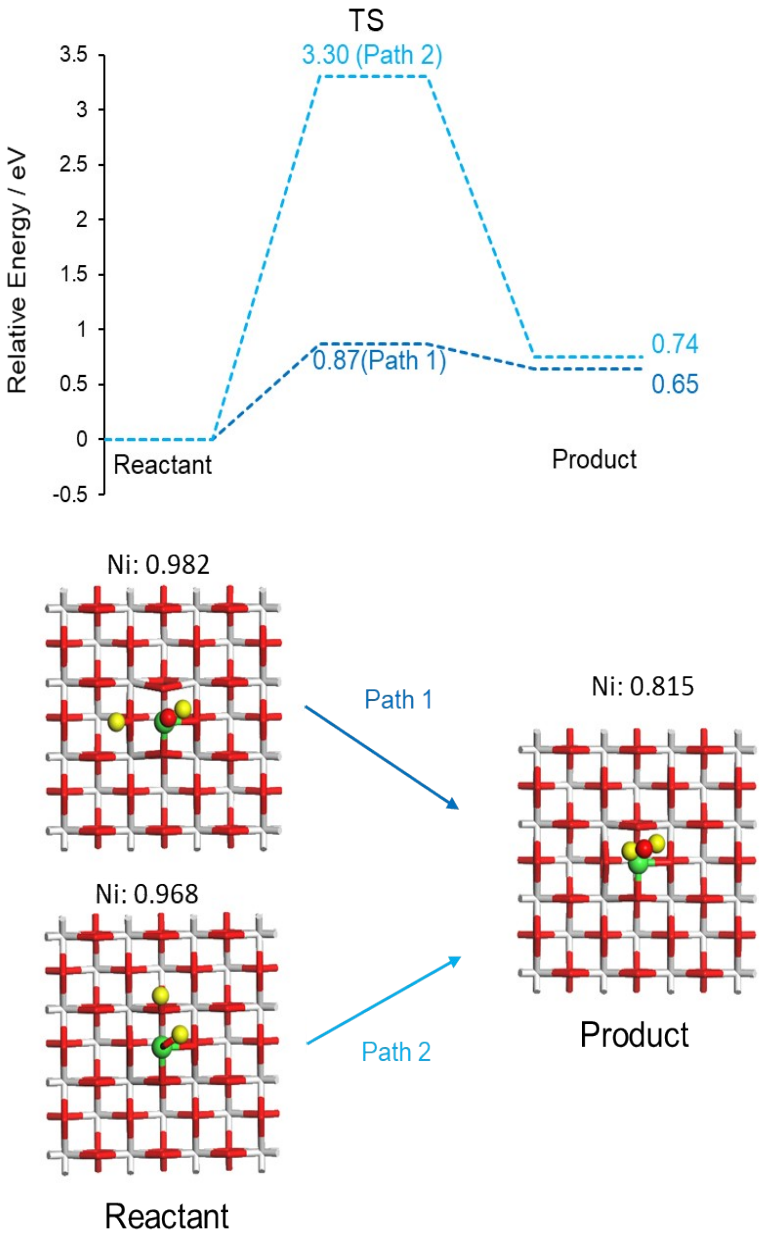

Fig. S24. Energy profiles and calculated model for reduction of Ni^{n+} by spilled H (Langmuir–Hinshelwood mechanism) (Step 4) on CeO_2(001). The values in the models are Mulliken atomic charges of Ni atom as determined by DFT calculations. Pale green ball (Ni), yellow ball (H), red stick (O), and white stick (Ce)

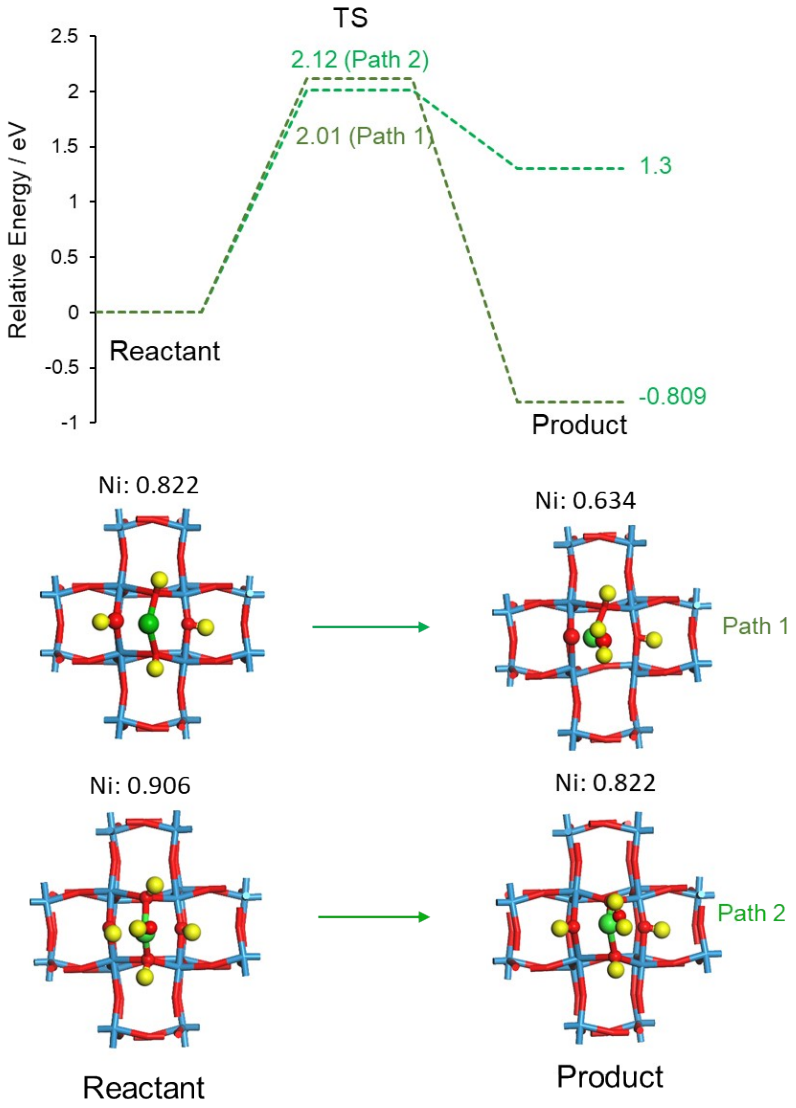

Fig. S25. Energy profiles and calculated model for reduction of Ni^{n+} by spilled H (Langmuir–Hinshelwood mechanism) (Step 4) on WO_3(001). The values in the models are Mulliken atomic charges of Ni atom as determined by DFT calculations. Pale green ball (Ni), yellow ball (H), red stick (O), and blue stick (W)

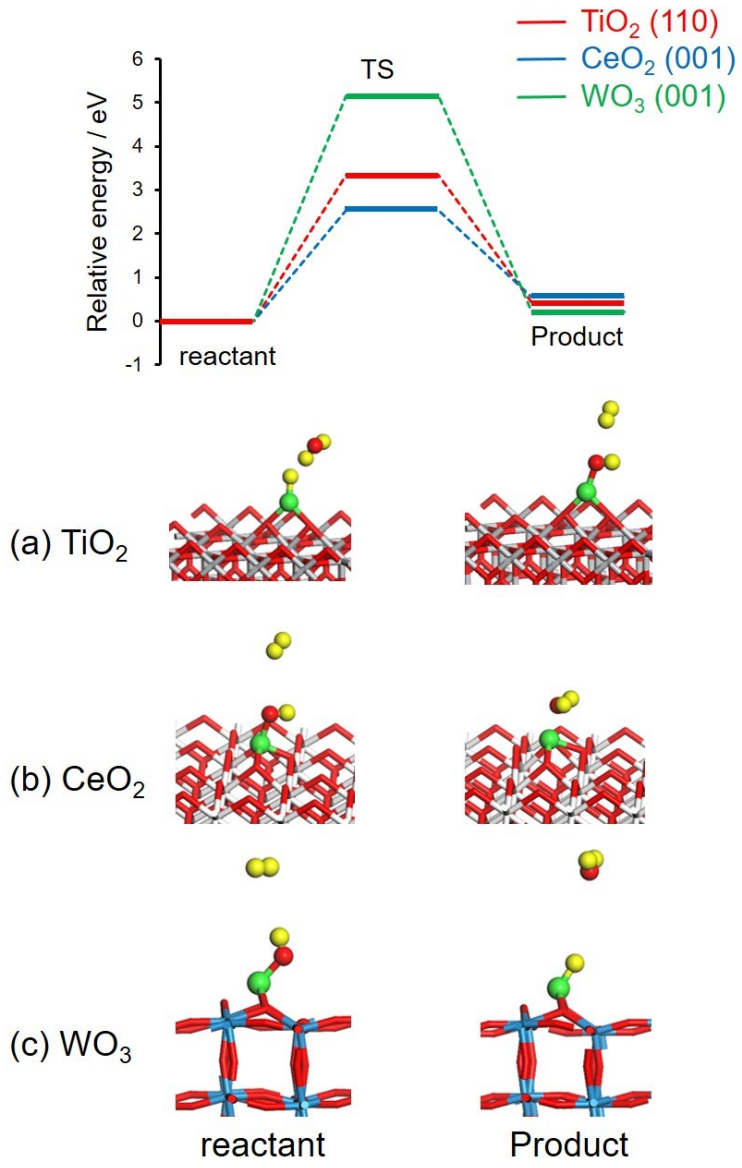

Fig. S26. Energy profiles and calculated models for reduction of Ni^{2+} species by vapor H_2 (Eley–Rideal mechanisms) on (a) TiO_2 (110), (b) CeO_2 (001), and (c) WO_3 (001).

Table S1. Comparison of binding energy of Ru_5 cluster and Ni atom on TiO_2 (110), CeO_2 (001), and WO_3(001).

model	Sample	metal	Binding Energy (eV)[a]
a	TiO_2	Ni	3.71
b	TiO_2	Ni	3.71
c	TiO_2	Ni	3.72
d	CeO_2	Ni	4.86
e	CeO_2	Ni	4.86
f	WO_3	Ni	2.42
g	WO_3	Ni	2.42

[a] Binding energy was defined by the equation $E_{metal} + E_{support} - E_{metal/support}$.

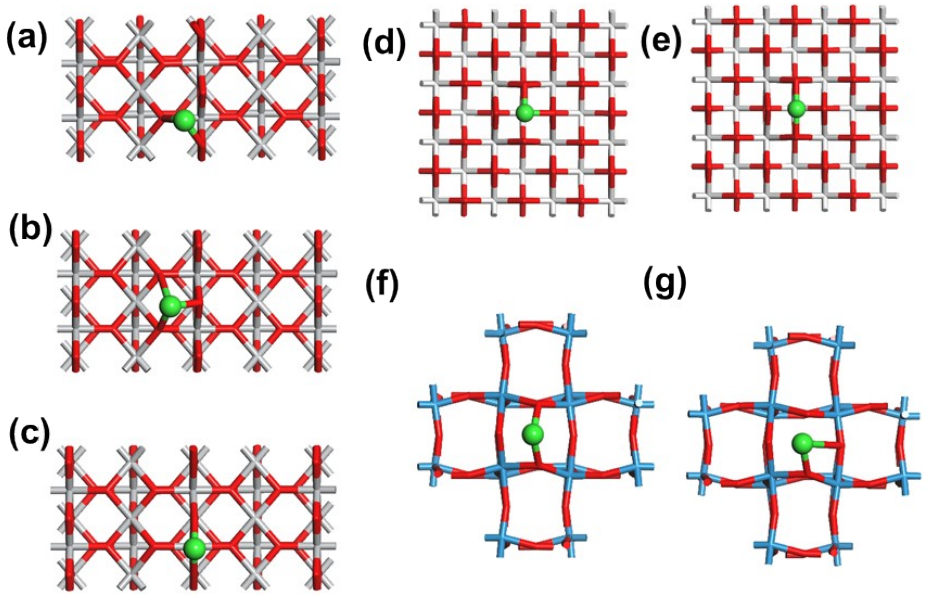

Fig. S27. Calculated model for rutile TiO_2 (110), CeO_2 (001), and WO_3(001).

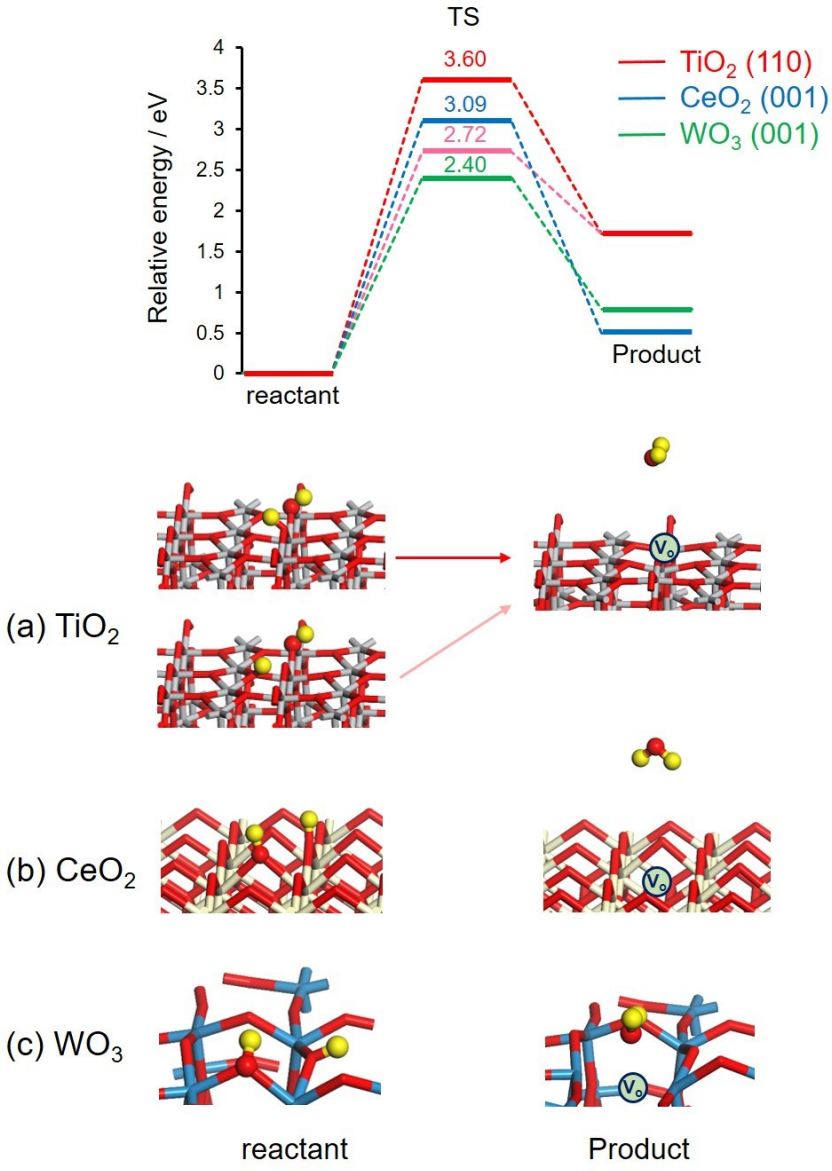

Fig. S28 Energy profiles and calculated models for removal of lattice oxygen by a spilled H atom to form H_2O and an oxygen vacancy on (a) TiO_2 (110), (b) CeO_2 (001), and (c) WO_3 (001). Yellow ball (H), red stick (O), gray stick (Ti), white stick (Ce), and blue stick (W).

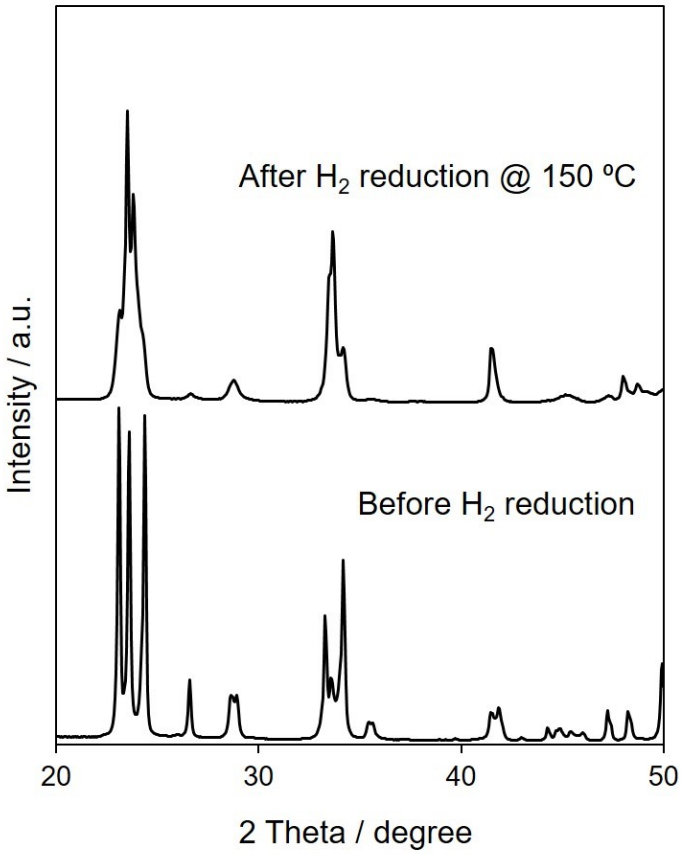

Fig. S29 XRD patterns of Ru/WO_3 before and after H_2 reduction.

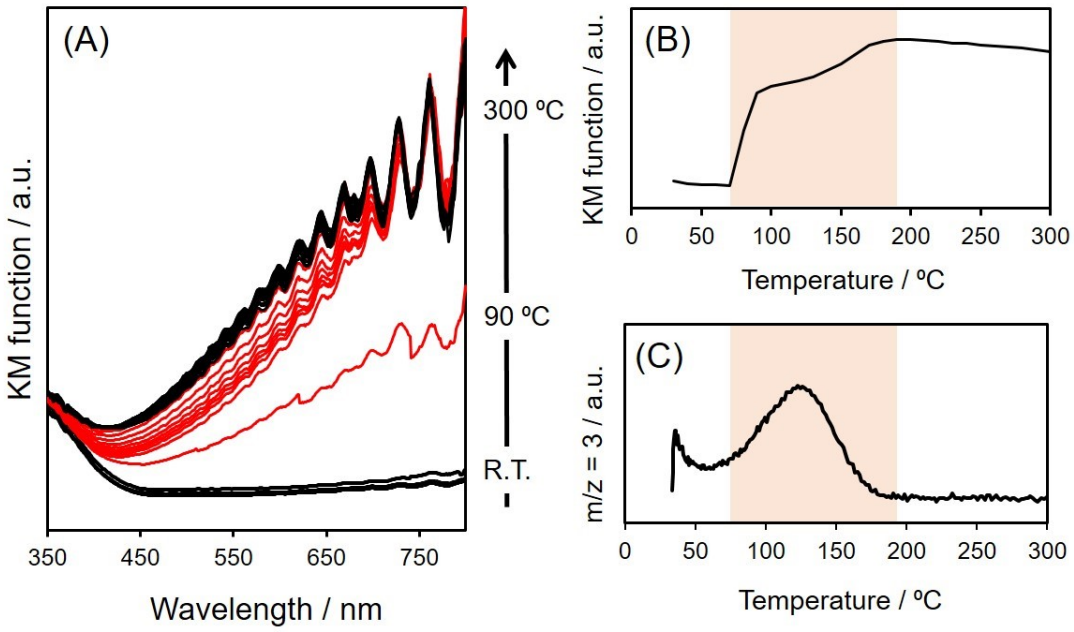

Fig. S30 (A) The increase of absorption in visible light region of Ru/WO_3 at elevated temperature under H_2 flow measured by *in situ* UV-vis instrument, (B) the plot of intensity of KM function at 600 nm as a function of temperature, (C) HD evolution monitored by mass spectroscopy for Ru/WO_3. The significant colour change from white to bronze (highlighted range in (B)) is due to the appearance of mixed valence transfer bands between W^{6+} and W^{5+}. This temperature range is matched well with that of the HD production peaks via H-D exchange (highlighted range in (C)).

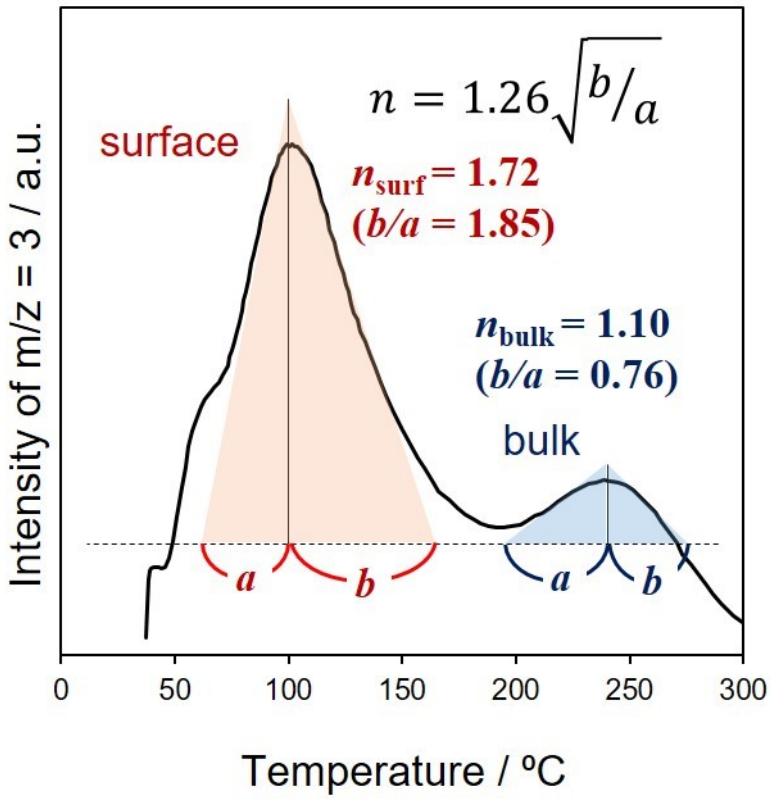

Fig. S31. The geometrical approach to obtain the reaction order (n_{surf} and n_{bulk}) from the result of MS measurement.

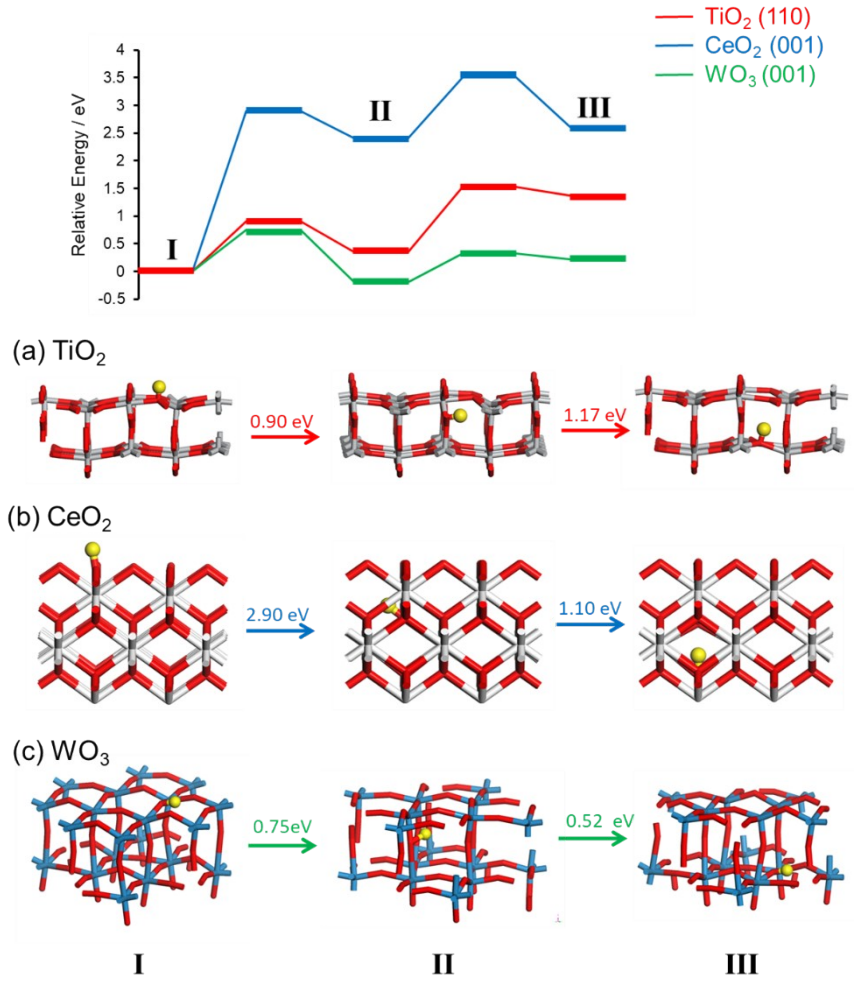

Fig. S32 Energy profiles and calculated models for H atom migration from the top surface to the first and second inside oxide layers on (a) TiO_2 (110), (b) CeO_2 (001), and (c) WO_3 (001). Yellow ball (H), red stick (O), gray stick (Ti), white stick (Ce), and blue stick (W).